Inorganic Chemistry

ARTICLE

pubs.acs.org/IC

Identification of a Single Light Atom within a Multinuclear Metal Cluster Using Valence-to-Core X-ray Emission Spectroscopy

Mario Ulises Delgado-Jaime,[†,‡] Benjamin R. Dible,[§] Karen P. Chiang,[§] William W. Brennessel,[§] Uwe Bergmann,[∥] Patrick L. Holland,[§] and Serena DeBeer*[,†,‡]

[†]Department of Chemistry and Chemical Biology, Cornell University, Ithaca, New York 14853, United States

[‡]Max-Planck-Institut für Bioanorganische Chemie, Stiftstrasse 34-36, D-45470 Mülheim an der Ruhr, Germany

[§]Department of Chemistry, University of Rochester, Rochester, New York 14627, United States

[∥]Linac Coherent Light Source, SLAC National Accelerator Laboratory, Menlo Park, California 94025, United States

Supporting Information

ABSTRACT: Iron valence-to-core Fe Kβ X-ray emission spectroscopy (V2C XES) is established as a means to identify light atoms (C, N, O) within complex multimetallic frameworks. The ability to distinguish light atoms, particularly in the presence of heavier atoms, is a well-known limitation of both crystallography and EXAFS. Using the sensitivity of V2C XES to the ionization potential of the bound ligand, energetic shifts of ~10 eV in the ligand 2s ionization energies of bound C, N, and O may be observed. As V2C XES is a high-energy X-ray method, it is readily applicable to samples in any physical form. This method thus has great potential for application to multimetallic inorganic frameworks involved in both small molecule storage and activation.

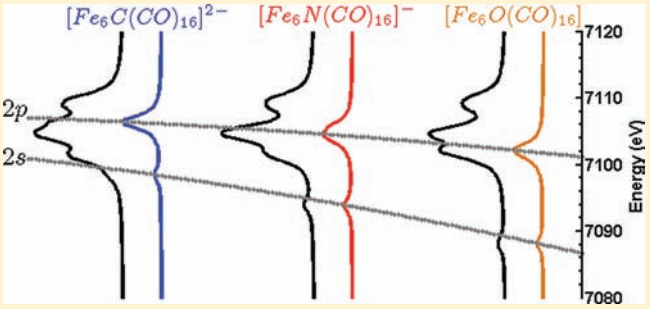

INTRODUCTION

The capture, conversion, and transport of small molecules (N_2, H_2, CO_2, CO) is of fundamental chemical interest. These processes include small molecule activation by both homogeneous and heterogeneous catalysts,[1−4] as well as gas storage by metal organic frameworks (MOFs).[5−8] The ability to identify the binding sites of light atoms to metals within these complex frameworks is essential to understanding their mechanisms and for optimizing material properties. However, the complex multimetallic nature of these systems presents significant challenges, both structurally and spectroscopically. X-ray crystallography is not reliable in these cases due to Fourier truncation artifacts. Neutron diffraction provides a means to determine light atom positions, but requires large sample volumes and is not amenable to the examination of complexes under *in situ* conditions. On the other hand, spectroscopy can provide corroborating evidence, but many spectroscopic techniques are complicated by paramagnetism and requirements for isotope substitution limit the application of vibrational spectroscopy. These challenges provide motivation for the development of new techniques that can reliably identify single light atoms within complex multimetallic systems.

Herein, we demonstrate the application of iron Kβ valence-to-core X-ray emission spectroscopy (XES) as a means to spectroscopically identify light atoms ligated to iron within a complex multinuclear metal framework, using the six iron cluster in tetramethylammonium carbidohexadecacarbonylferrate (2−), $(NMe_4)_2[Fe_6C(CO)_{16}]$, as a reference. The V2C of an XES spectrum involves transitions originating from *occupied* valence MOs. On the basis of previous studies, the mechanism for intensity should derive from Fe *n*p character into ligand-based MOs.[9,10] Therefore, provided there is significant interaction with the iron *n*p orbitals, specific XES transitions from the carbon-center-based MOs are expected. Recently, in XES studies of simple mononuclear ferrous and ferric complexes, we have shown that the V2C region of the spectrum provides a sensitive probe of metal−ligand bond distances as well as ligand identity.[9] It has also previously been demonstrated that this region of the spectrum can be well modeled utilizing a relatively simple one-electron DFT framework.[9,11−14] In the present study, we highlight the sensitivity of XES for detecting a single light atom in a complex six iron cluster. We begin by reinvestigating the crystallography of $(NMe_4)_2[Fe_6C(CO)_{16}]$ and also closely examining the XAS and EXAFS. A correlation of XAS and EXAFS data to theory is presented in order to understand the limitation of these methods for the determination of ligated light atoms. Parallel correlations of the experimental V2C XES data to theory highlight the sensitivity of this method. This study lays the groundwork for the application of V2C XES to iron clusters in biological and chemical catalysis.

METHODS

Synthesis. The compound $(NMe_4)_2[Fe_6C(CO)_{16}]$ was synthesized according to the literature.[15] The ^{13}C NMR spectrum of the

Received: May 31, 2011
Published: September 28, 2011

compound was not reported in that paper, but we recorded it in order to verify the presence of a central carbide. $^{13}C\{^{1}H\}$ NMR (125.7 MHz, THF-d_8): δ 56 (CH_3), 229 (CO), 485 (C^{4-}) ppm. The ratio of the integrations of the peaks at 229 and 485 was roughly 16:1, as expected.

Crystallography. A black crystal of $(NMe_4)_2[Fe_6C(CO)_{16}]$ was placed onto the tip of a glass fiber and mounted on a Bruker SMART Platform diffractometer equipped with an APEX II CCD area detector. Data were collected at 293(2) K [**RT**] and 100.0(1) K [**LT**] using Mo Kα radiation (graphite monochromator).[16] The crystal structure of **LT** required twin modeling. Crystallographic details are given in the Supporting Information.

XAS. The Fe K-edge XAS data were recorded at the Stanford Synchrotron Radiation Lightsource (SSRL) on focused beamline 9-3, under ring conditions of 3 GeV and 60−100 mA. A Si(220) double-crystal monochromator was used for energy selection, and a Rh-coated mirror (set to an energy cutoff of 10 keV) was used for harmonic rejection. Internal energy calibration was performed by assigning the first inflection point of the Fe foil spectrum to 7111.2 eV. The samples were prepared by dilution in boron nitride, pressed into a pellet, and sealed between 38 μm Kapton tape windows in a 1 mm aluminum spacer. An Oxford Instruments CF1208 continuous flow liquid helium cryostat was used to maintain samples at temperatures of 20 K during data collection. The data were measured in transmission mode to $k \sim 15$ Å^{-1}. No evidence of photoreduction was observed during the course of data collection.

The data were calibrated and averaged using EXAFSPAK.[17] Pre-edge subtraction and splining were carried out using PYSPLINE.[18] A three-region cubic spline of order 2, 3, 3 was used to model the smooth background above the edge. Normalization of the data was achieved by subtraction of the spline and normalization of the postedge region to 1. The resultant EXAFS was k^3-weighted to enhance the impact of high-k data. Theoretical EXAFS signals (k) were calculated using FEFF[19] (version 8.0). XANES data were fit using Blueprint XAS.[20,21] XANES spectra were calculated with FEFF 9.0 and the jFEFF GUI.[22]

XES. All samples were prepared as dilutions in boron nitride, pressed into 1 mm Al spacers, and sealed with 38 μm Kapton tape in an inert atmosphere glovebox. Samples were mounted in continuous flow liquid helium cryostat to maintain samples at temperatures of 20 K during data collection. XES data were, then, collected at the SSRL beamline 6-2 (54-pole wiggler, 1 T). The incident energy was set to 9 keV utilizing a Si(111) liquid-nitrogen cooled monochromator. Vertical and horizontal focusing mirrors were used to achieve a beam size of 200 × 800 μm^2 with a flux of ~4 × 10^{12} photons/s at 100 mA. The energy of the incident beam was calibrated with an iron foil, setting the first inflection point to 7111.2 eV.

XES spectra were recorded with a crystal array spectrometer, which employs three spherically bent Ge(620) crystals (100 mm diameter, 1 m radius of curvature) aligned on intersecting Rowland circles.[23] An energy resolving Si drift detector (Vortex) with a 3 mm vertical slit was used as the X-ray photon detector. Samples were positioned at 45° with respect to the incident beam and were maintained at a temperature of 20 K in an Oxford CF1208 continuous flow cryostat. A helium-filled flight path was utilized between the cryostat and the spectrometer to minimize signal attenuation. Iron Kβ XES spectra were collected from 7020 to 7120 eV, with a step size of +0.2 eV over the K$\beta_{1,3}$ main line (7020−7070 eV) and steps of +0.15 eV over the valence to core region (7070−7120 eV). Spectra were normalized to the incident flux I_0 measured in a He-filled ion chamber. The spectrometer energy was calibrated by measuring the energy of the elastically scattered beam as a function of spectrometer position. The incident beam monochromator was calibrated by assigning the first inflection point of an Fe K-edge foil spectrum to 7111.2. Fe_2O_3 was used as a reference sample for calibrating the spectrometer energy between different experimental runs, with the maximum of the K$\beta_{1,3}$ and K$\beta_{2,5}$ lines calibrated to 7060.6 and 7107.2 eV, respectively.

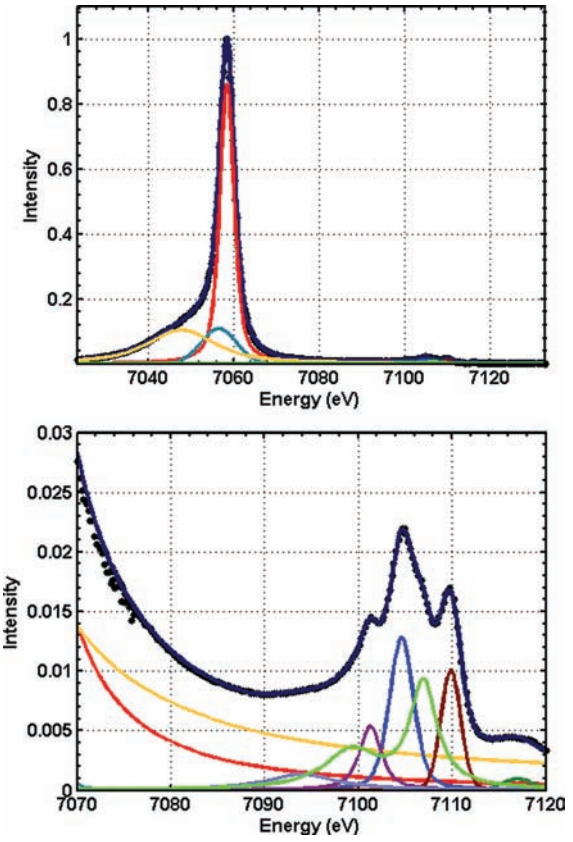

Figure 1. Representative fit showing, in the Kβ main line region (top) and the V2C region (bottom), the model used for the fitting of the experimental Fe Kβ XES data of $(NMe_4)_2[Fe_6C(CO)_{16}]$. The plot shows the raw data. The normalization and background subtraction are done in conjunction with fitting.

XES data were fit using a mathematical model implemented in Blueprint XAS and graphically shown in Figure 1:

$$f_T = f_{K\beta} + f_{V2C} + f_{Mult} + I_{of} \quad (1)$$

$$f_{K\beta} = I_T \cdot N \cdot I_{V2C} \sum_{j=1}^{3} B_j \cdot ((1 - G_{j,K\beta}) \cdot f_{L,j,K\beta} + G_{j,K\beta} \cdot f_{G,j,K\beta}) \quad (1.a)$$

$$f_{V2C} = I_T \cdot I_{V2C} \sum_{i=1}^{N=5,6} A_i \cdot ((1 - G_{i,V2C}) f_{L,i,V2C} + G_{i,V2C} f_{G,i,V2C}) \quad (1.b)$$

$$f_{Mult} = I_{Mult}((1 - G_{Mult}) f_{L,Mult} + G_{Mult} f_{G,Mult}) \quad (1.c)$$

$$f_{L_\alpha,X} = \frac{\gamma_\alpha, X}{\pi(\gamma_\alpha, X^2 + (x - E_\alpha, X)^2)}$$

$$f_{G_\alpha,X} = \frac{\sqrt{\ln 2}}{\gamma_\alpha, X\sqrt{\pi}} e^{-\ln 2(x - E_\alpha, X)^2/2\gamma_\alpha, X^2}$$

In this model, the normalized intensity of the entire V2C region is set as one of the fit parameters (I_{V2C}). The individual intensity (i.e., total area) of each of the 6 (or 5) features (Figure 1, bottom) of this region is defined as a fraction of I_{V2C} (A_i, eq 1.b). Moreover, the intensity of the Kβ main line envelope (that is, K$\beta_{1,3}$ + Kβ') is modeled as a multiple N of I_{V2C} ($N \cdot I_{V2C}$, eq 1.a), whereas the intensity area of each of the three individual features is set as fractions (B_j, eq 1.a) of this. The data are normalized within the fitting procedure by defining a normalization

dx.doi.org/10.1021/ic201173j |Inorg. Chem. 2011, 50, 10709–10717

Table 1. Selected Bond Lengths [Å] and Angles [deg] in RT and LT as Thermal Ellipsoid Plots Represented at 50% Probability Density[a]

LT (~100 K)		RT	
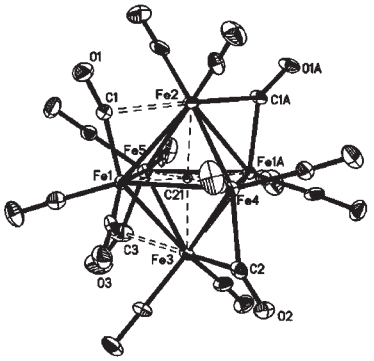		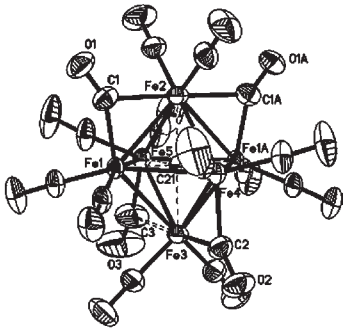	
Fe2—C1	2.234(5)	→	2.523(8)
Fe2—C1A	2.234(5)	→	1.964(7)
Fe3—C2	2.075(6)		2.018(8)
Fe3—C3	2.510(9)		2.561(10)
Fe7—C11	2.226(5)	→	1.982(7)
Fe7—C11A	2.226(5)	→	2.434(9)
Fe8—C12	1.958(7)		1.961(8)
Fe8—C13	2.611(6)		2.585(8)
Fe1—C1—O1	150.2(4)	→	164.0(7)
Fe1A—C1A—OA	150.2(4)	→	138.1(6)
Fe4—C2—O2	142.0(6)		140.4(6)
Fe5—C3—O3	162.7(9)		163.1(9)
Fe6—C11—O11	150.5(4)	→	140.7(6)
Fe6A—C11A—O11A	150.5(4)	→	159.4(8)
Fe9—C12—O12	138.7(6)		138.5(7)
Fe10—C13—O13	166.1(6)		165.4(8)

[a] Arrows indicate lengths that change from the reduction of cluster symmetry.

condition, where

$$10^3 \cdot I_T = I_T \cdot I_{V2C}(1 + N(B_1 + B_2 + B_3))$$

The factor 10^3 is used for consistency with previous studies where the total area was set to 1000[9]. Note that the intensities of the high energy features occurring above 7111 eV (presumably due to multiple electron excitations[23]) are not included in the total area (I_T), nor is a small offset (I_{of}) which is used to zero the baseline in the fits.

Using this model, a total of 20 reduced-bias good fits were obtained by using the previously reported methodology[24] as implemented in Blueprint XAS.[20,21] The results of relevant parameters are provided in Table S8.

DFT Calculations. All calculations were performed with the ORCA quantum chemistry program[25] using the theoretical protocol summarized elsewhere.[9,26] Geometry optimizations were calculated using the experimental X-ray structure of the $(NMe_4)_2[Fe_6C(CO)_{16}]$ cluster at 100 K and, when applicable, by substituting the central μ_6 atom by N or O. Geometry optimizations were performed using the gradient-corrected functional model for exchange by Becke[27] and the gradient-corrected model for correlation by Perdew[28,29] (BP86), following the model potential implementation of van Wüllen,[30] and the scalar-relativistically recontracted def2-TZV/J basis set. Single point calculations with XES and XAS were performed with the BP86 functional in conjunction with the CP(PPP) basis[31] for the Fe atom (with a special integration accuracy of 7) and the TZVP basis set for all other atoms. These calculations were carried out with a dense integration grid (ORCA Grid4) in a dielectric continuum using the conductor-like screening model (COSMO)[32] in an infinite dielectric. Finally, the deconvolution of the calculated XES data, from DFT, was accomplished using MOAnalyzer,[33] and molecular orbitals were visualized using Chimera.[34]

In addition to ORCA calculations of the XAS pre-edge region, full multiple scattering XANES calculations were carried out using FEFF 9.0.[19,35] XANES calculations were carried out at the crystallographic coordinates (of the $[Fe_6C(CO)_{16}]^{2-}$ structure) and ORCA optimized structures of $[Fe_6C(CO)_{16}]^{2-}$, $[Fe_6N(CO)_{16}]^{1-}$, $[Fe_6O(CO)_{16}]^{0}$. In all cases a Hedin Lundqvist potential was utilized. The effect of total complex charge was investigated, but was not found to have a significant effect. A constant shift of −6 eV was applied to all FEFF calculated

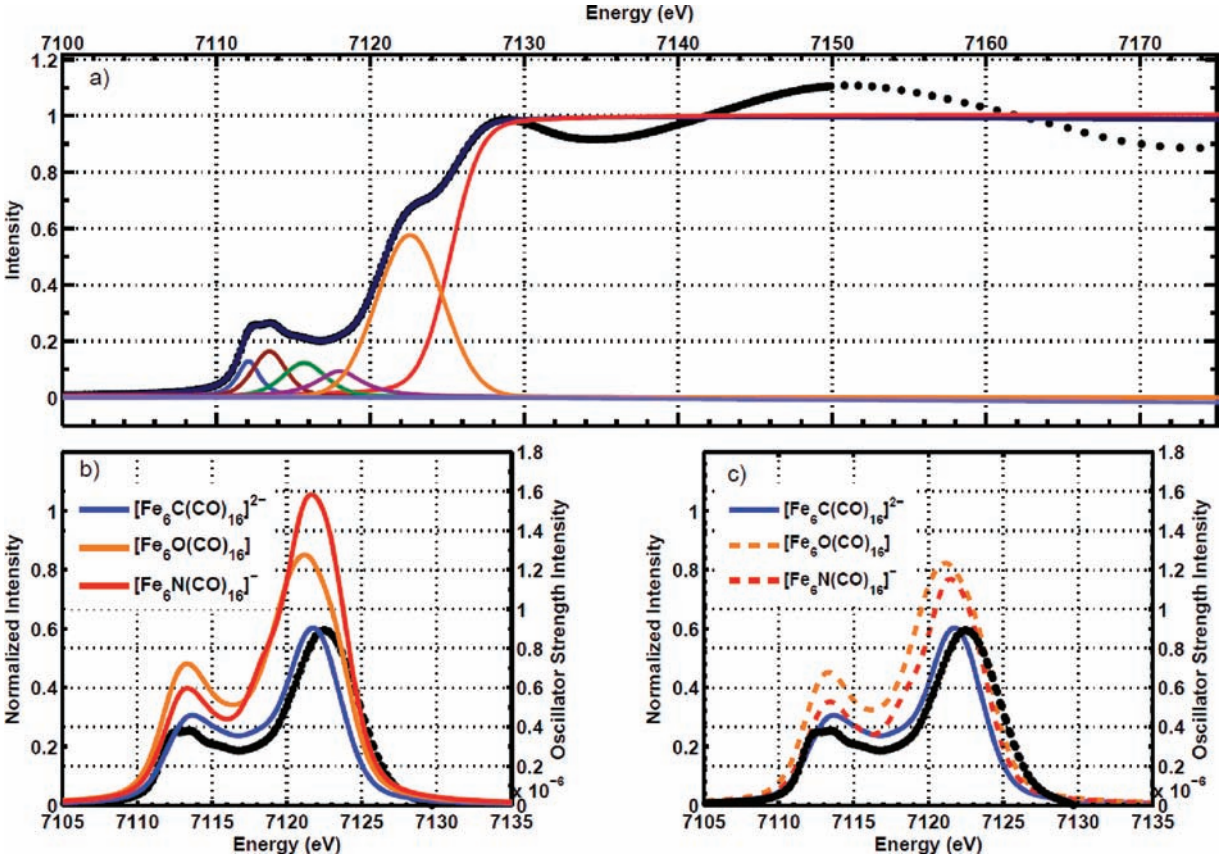

Figure 2. (a) Representative fit to experimental Fe K-edge XAS data of $[Fe_6C(CO)_{16}](NMe_4)_2$. (b) Comparison of experimental Fe K pre-edge XAS data of $[Fe_6C(CO)_{16}](NMe_4)_2$ to the DFT-calculated spectra of $[Fe_6C(CO)_{16}]^{-2}$, $[Fe_6N(CO)_{16}]^{-}$, and $[Fe_6O(CO)_{16}]$ based on the optimized structure of $[Fe_6C(CO)_{16}]^{-2}$. (c) Comparison of experimental Fe K pre-edge XAS data of $[Fe_6C(CO)_{16}](NMe_4)_2$ to the DFT-calculated spectra of geometry optimized $[Fe_6C(CO)_{16}]^{-2}$, $[Fe_6N(CO)_{16}]^{-}$, and $[Fe_6O(CO)_{16}]$. The Fe K pre-edge XAS data in parts b and c are obtained by subtracting the fit background (light blue line in part a) and the fit edge (red line in part a). For all DFT-calculated spectra, the following simulation parameters were used in parts b and c: 1.5 eV broadening (hwhm), 182.1 eV (energy shift), 3:2 (Lorentzian:Gaussian ratio). The individual calculated XES transitions and the corresponding spectra with reduced broadening (0.6 eV of hwhm) are shown in Figures S3−S5.

spectra. The many body reduction factor (S_0^2) was set to 1.0. The default core hole broadening was utilized for spectral plots, with no additional experimental broadening.

RESULTS AND DISCUSSION

Crystallography. The compound under investigation here, tetramethylammonium carbidohexadecacarbonylferrate(2−), $(NMe_4)_2[Fe_6C(CO)_{16}]$, was previously characterized in 1971 with a low-resolution, room-temperature crystal structure in the space group *Pnma*.[15,36] We reproduced this **RT** structure with an *R*1 value of 5.1%, solving in the space group *Pnmb*, a nonstandard setting of *Pnma*, in order to facilitate comparison to **LT**. In the asymmetric unit of **RT** there are two independent iron anion clusters that are bisected by crystallographic mirror planes (thus one-half of each is unique) and two independent tetramethylammonium cations with atoms in general positions. Interestingly, cooling the same crystal to 100 K caused a phase change to a new structure (**LT**) in space group $P2_1/n$ with resolvable nonmerohedral twinning. The phase change was reversible, occurring at ∼200 K. In **RT**, each cluster has two orthogonal pairs of bridging or near-bridging carbonyl ligands that have an iron atom common to each pair. One of these pairs has identical Fe−C(carbonyl) distances due to the mirror symmetry, while the other is highly asymmetric. According to Table 1, the mirror symmetry in **RT** is evident with Fe2−C1 = Fe2−C1A = 2.234(5) Å. However, in **LT** due to a reversible phase change around ∼200 K, the mirror symmetry is broken and *both* Fe−C distances within each pair show significant asymmetry with Fe2−C1 = 2.523(8) and Fe2−C1A = 1.964(7) Å. In both cases, the Fe2−C2 and Fe2−C3 bonds are inequivalent at both temperatures, but the symmetry breaking is apparent also in the Fe−C−O angles (see Table 1 for details). Despite the differences in coordination, the iron environments are similar, as shown by Mössbauer spectroscopy.[37]

It is notable that the crystallography does not clearly distinguish the identity of the central atom in this hexairon cluster. As often observed for atoms that lie on a crystallographic symmetry element, the refined thermal parameters for the central carbon atom are somewhat smaller than other atoms in the structure. This phenomenon prevents reliable identification of the central atom with crystallography, despite the excellent *R* value. Because this compound is diamagnetic, it is possible to verify the identity of the central atom by ^{13}C NMR spectroscopy (singlet at δ 485 ppm, a chemical shift that is characteristic of carbides). Note that NMR spectroscopy is not possible for clusters with central atoms that are not NMR-active, or when the cluster is paramagnetic. This highlights the need for

dx.doi.org/10.1021/ic201173j |*Inorg. Chem.* 2011, 50, 10709–10717

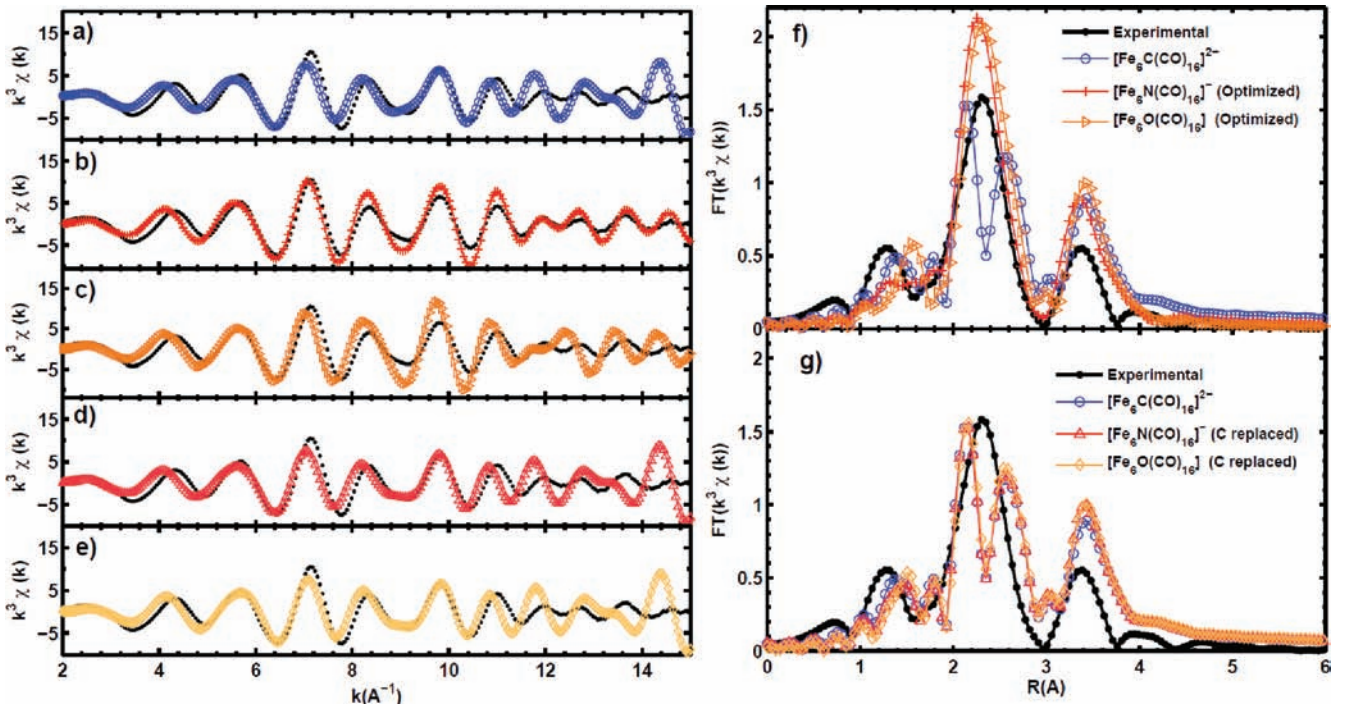

Figure 3. Comparison of the FEFF calculated EXAFS for $[Fe_6C(CO)_{16}]^{2-}$ (blue, a), $[Fe_6N(CO)_{16}]^{-}$ (red, b), and $[Fe_6O(CO)_{16}]$ (yellow, c) to k^3-weighted of the experimental Fe K-edge EXAFS spectrum of $[Fe_6C(CO)_{16}]^{2-}$ (black dotted lines). The geometries used for the FEFF calculated EXAFS correspond to the optimized structures of each cluster, while the corresponding Fourier transforms are shown in part f. The structures used for parts d and e are all identical to an optimized $[Fe_6C(CO)_{16}]^{2-}$, with the central atom replaced by N or O in parts d and e, respectively. The corresponding Fourier transforms of parts d and e are shown in part g.

alternative methods (like XES) to identify central atoms in clusters.

XAS and EXAFS Studies. In addition to crystallography and XES experiments (discussed below), the sensitivity of XAS to changes in the identity of a single light atom was assessed.

Figure 2a shows the full XANES region, together with the fit to the background that was used to produce the data shown in Figure 2b,c. Figure 2b,c shows a comparison between the experimental Fe K pre-edge XAS spectrum of $(NMe_4)_2[Fe_6C(CO)_{16}]$ and the calculated Fe K pre-edge XAS spectra for $[Fe_6C(CO)_{16}]^{2-}$, $[Fe_6N(CO)_{16}]^{-}$, and $[Fe_6O(CO)_{16}]$, using a previously described protocol (see also Figures S3−S5 for simulated spectra with reduced broadening).[26] The fragment decomposition of the DFT-calculated XAS (Figures S3−S5; Tables S3−S7) in each case indicates that the features ∼7115 are primarily due to transitions to unoccupied iron-3d and π^*-CO based MOs, the features between 7115 and 7120 are due to transitions to unoccupied iron-4p based MOs, and the features ∼7120 eV are due to transitions to σ^*CO-based MOs. As might be anticipated, no feature can be associated directly with the central species (C^{4-}, N^{3-}, or O^{2-}). We note from our ORCA calculations that the increased intensity for the N and O species is not simply a result of the structural changes. In fact when single point calculations for the N- and O-based clusters are performed using the $[Fe_6C(CO)_{16}]^{2-}$ optimized structure as the reference geometry for DFT, the trend is even more pronounced. We suggest that the differences in total intensity are due to an inherently greater intensity specific to Fe−O (and especially to Fe−N bonding interactions), as has been previously observed in monomeric iron oxo and nitrido complexes.[38] Despite the differences in the pre-edge intensities and energy distribution, as revealed by Figures S3−S5, the intensity mechanism is indirect and therefore does not allow for a means to directly detect differences in bound light atoms. It does, however, provide a complementary information to the V2C XES data.

We note that XANES calculations were also carried out using the multiple scattering approach as implemented in FEFF 9.0 (see Figure S2). These calculations also show sensitivity to the nature of the central atom. However, in contrast to the DFT calculations which model the pre-edge region reasonably well in the $[Fe_6C(CO)_{16}]^{2-}$ limit, none of the FEFF calculations produce particularly good agreement with the experimental data. For this reason we chose to focus on the results using a one-electron DFT based approach as implemented in ORCA, and to focus on the V2C XES and pre-edge XAS data.

The EXAFS region of the XAS spectrum was also investigated. Figure 3 presents the experimental data compared to the FEFF calculated spectra using the optimized geometry for $[Fe_6C(CO)_{16}]^{2-}$ (a), $[Fe_6N(CO)_{16}]^{-}$ (b), and $[Fe_6O(CO)_{16}]$ (c). All of the calculated EXAFS spectra are very similar at $k < 11$ Å^{-1}, but at high k, significant differences become apparent (see Figure 3a−c). The corresponding Fourier transforms are given in Figure 3f. Here it is of interest to note that despite being crystallographically well-characterized the calculated EXAFS do not agree well with the experimental data. This likely reflects a limitation in the modeling of the disorder parameters. Considerably better agreement with experiment is achieved by allowing these parameters to refine. In any case, we note that the subtle differences at high k cannot readily be attributed to the identity of the central atom, but are more likely structural in origin. This can be verified by using the same coordinates to calculate the EXAFS for all three cluster models and only changing the identity of the central atom. In this case, the FEFF calculated EXAFS (Figure 3a,d,e)

dx.doi.org/10.1021/ic201173j |*Inorg. Chem.* 2011, 50, 10709–10717

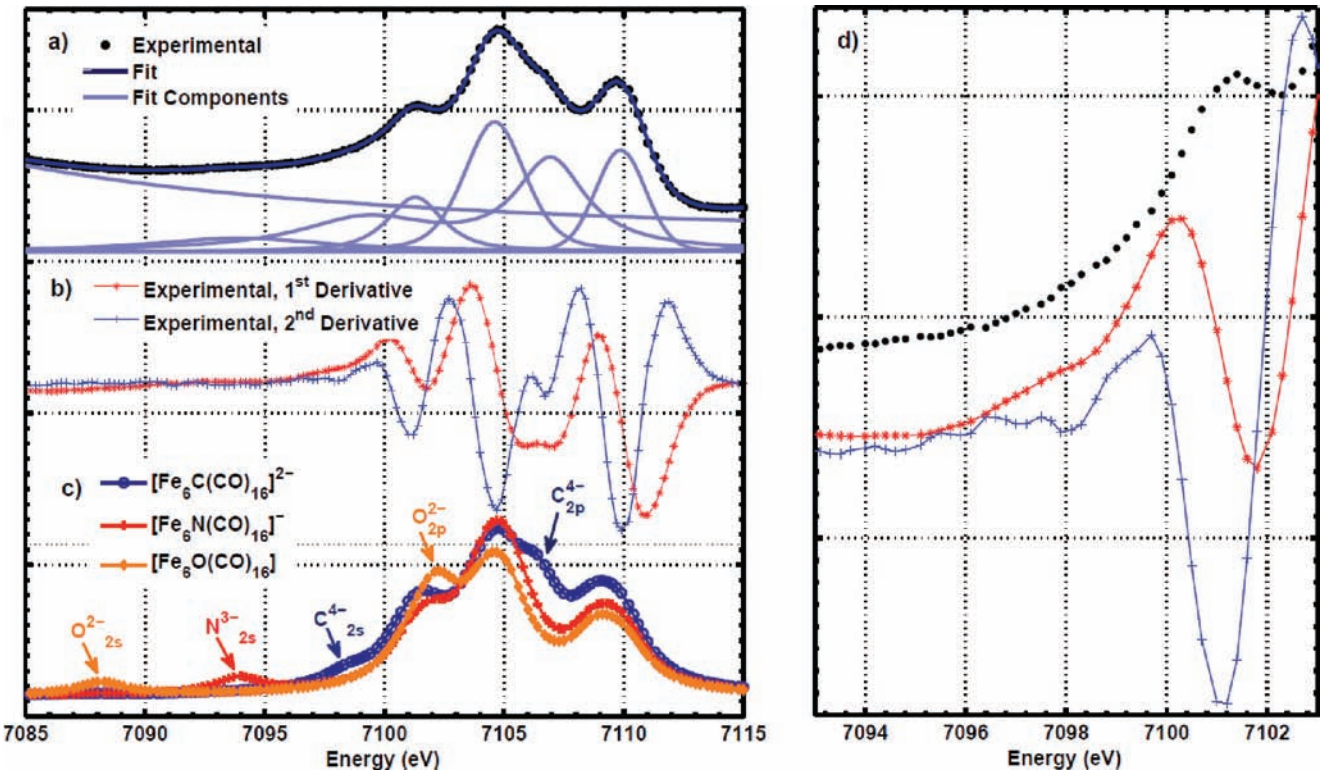

Figure 4. Experimental and theoretical results for the analysis of the V2C Fe Kβ XES data of $[Fe_6C(CO)_{16}]^{2-}$. (a) Representative six-peak fit to the experimental data; the background corresponds to the "tail" of the Kβ main line. (b) Smoothed first and second derivatives of the experimental data. (c) Calculated spectra from optimized $[Fe_6C(CO)_{16}]^2$, $[Fe_6N(CO)_{16}]$, and $[Fe_6O(CO)_{16}]$ structures simulated using Lorentzian functions with parameters 1.2 eV (hwhm), 181.6 eV (energy shift), and 7.2 (scaling factor). (d) Experimental V2C Fe Kβ XES data for $[Fe_6C(CO)_{16}]^{2-}$ and corresponding smoothed first and second derivatives in the energy region 7093−7103 eV. The *y*-axes correspond to (a) normalized intensity, (b) derivative, and (c) calculated intensity. The axis in part d has been scaled to allow the normalized data and derivative to be plotted on the same scale.

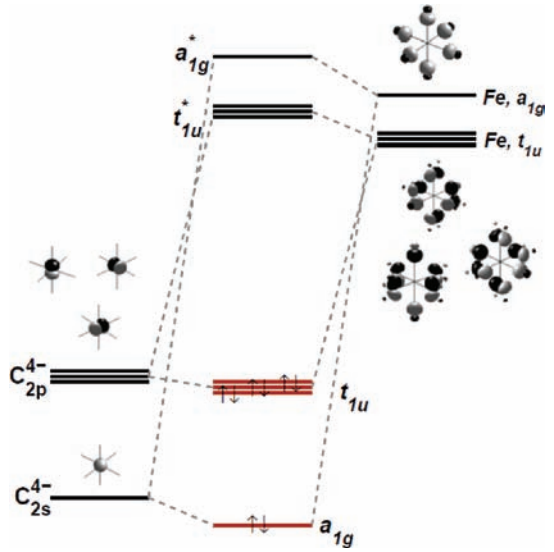

Figure 5. Partial MO diagram of $[Fe_6C(CO)_{16}]^{2-}$ depicting the interaction of the central octahedral carbon atom with SALCs of the surrounding iron atoms.

(EXAFS) and the corresponding Fourier transforms (Figure 3g) are essentially identical.

V2C XES. Figure 4a presents the Fe Kβ XES spectrum at 20 K (corresponding to the **LT** structure) for $(NMe_4)_2[Fe_6C(CO)_{16}]$ together with a representative fit. To qualitatively interpret these data, we have derived a frontier-orbital picture of the cluster, using elementary group theory, allowing for the interaction of the 2s and 2p orbitals of the central carbon with the iron fragments.[39−41] The C(2s) orbital interacts with an a_{1g} symmetry adapted linear combination of orbitals (SALCs) from the surrounding iron atoms while the C(2p) orbitals interact with iron-based t_{1u} SALCs (Figure 5).[39] The bonding combination from these interactions should then correspond to carbon-based filled MOs in agreement with the valence-bond picture of a carbide (C^{4-}).

On the basis of this simple MO-based assessment (Figure 5), transitions originating from the carbide 2p-based MOs (t_{1u}) should lie in the higher-energy region of the spectrum (7100−7110 eV; Figure 4a), while the carbide 2s-based MO (a_{1g}) should appear at lower energy (7095−7100 eV, Figure 4a). In this multifeatured spectrum, however, additional contributions are expected from carbonyl-based orbitals interacting with the iron 4p orbitals.[10] From the experimental data and the smoothed first and second derivatives of it, a total of 6 peaks are required to fit the data (Figure 4a,b,d). To assign these contributions, the spectrum of $[Fe_6C(CO)_{16}]^{2-}$ was calculated using a protocol described previously.[9]

A similar fitting model with only 5 peaks was also used to obtain another family of 20 fits. The excellent agreement between theory and experiment, when using a 6 peak model (see Figures S6 and S7), supports the assignment of C^{4-}2s and C^{4-}2p contributions to the spectrum (Figure 4a,c). Remarkably,

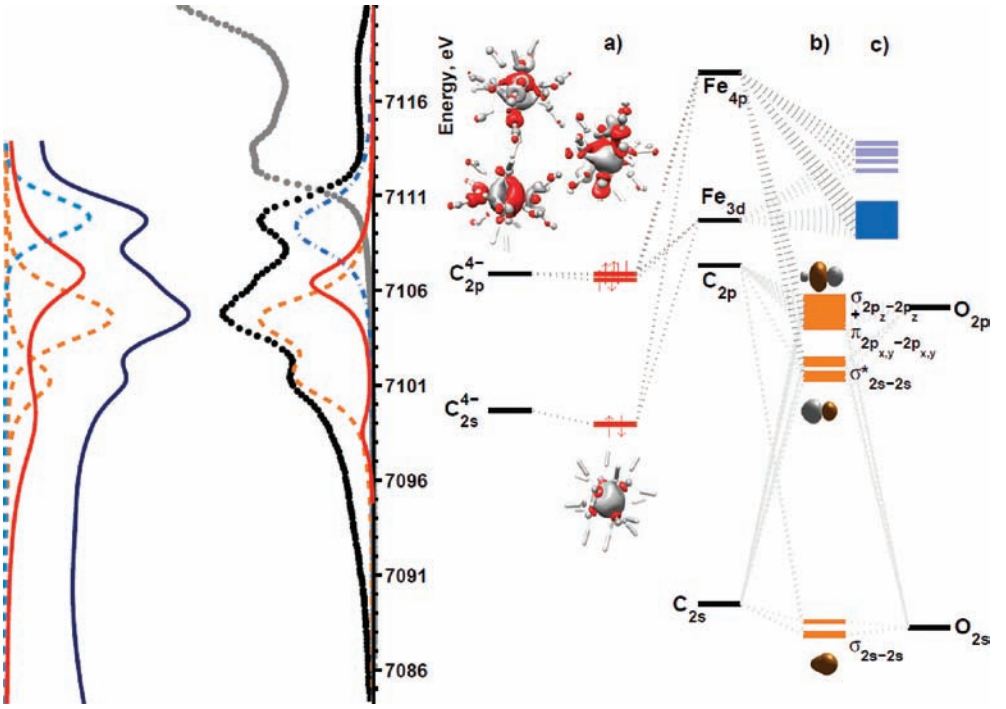

Figure 6. Fragment decomposition of the experimental V2C Fe Kβ XES using DFT. The calculated projections (center) of (a) carbide-based MOs (red solid line), (b) carbonyl-based MOs (orange dashed line), and (c) Fe-3d based MOs (blue dash-dotted line) are shown together with the experimental XES data (black dots) and experimental XAS (gray dots) on the same scale. These projections are also consistent with fits to the experimental XES data (far left). For simplicity, arrows representing electrons in parts b and c have been omitted; however, all carbonyl-based MOs shown in part b represent filled MOs whereas Fe-3d based MOs shown in part c have been colored in different shades of blue depending on occupancy.

the simple interaction scheme depicted in Figure 5 between the carbide and iron atoms seems to correctly represent the dominant interactions that dictate the calculated electronic structure of the carbide-based MOs (see also Figure 6a). Importantly, we note that the calculated XES spectra show the same relative number and positions of features regardless of the structure used (experimental or geometry optimized, see Figure S8 in Supporting Information). It is of interest to note, however, that the relative intensity of the V2C XES features do change slightly with structural variations, with the strongest agreement between experiment and theory corresponding to the **LT** crystal structure. This is consistent with our XES data collection being performed at low temperature and below the temperature of the phase change to the **RT** structure.

In order to probe the sensitivity of this method to the identity of the interstitial μ_6 atom, we then calculated spectra for hypothetical $[Fe_6N(CO)_{16}]^-$ and $[Fe_6O(CO)_{16}]$ complexes (Figure 4c). These comparisons show a dramatic shift in the ligand 2s ionization energy from ~7098 to ~7094 to ~7088 eV, for C, N, and O, respectively. Previously, similar trends have been observed experimentally for Mn- and Cr-containing complexes.[12,42,43] Collectively, it has been observed, here and in previous studies,[9,12,42,43] that the intensity of this feature, which appears less intense and broader than the rest of the V2C envelope, is, nevertheless, consistently observed experimentally (see Figure 3d) for ligands consisting of a single atom such as in C^{4-}, N^{3-}, or O^{2-}. However, when the light atom is part of a larger ligand framework, the delocalization of the 2s electron density across the ligand may reduce the XES intensity.

In addition, parallel shifts are observed to higher energy which correspond to the changes in the 2p ionization energy. However, we note that the overlap between the 2p central-atom-based features and the 2p carbonyl-based features require spectral fragment decomposition in order to assess their relative contributions. In this sense, the 2s features provide an isolated and unambiguous experimental probe of the identity of the bound ligand. These observations are also preserved when $[Fe_6N(CO)_{16}]^-$ and $[Fe_6O(CO)_{16}]$ are calculated at the same coordinates as the optimized $[Fe_6C(CO)_{16}]^{2-}$ structure (Figure S9 in Supporting Information), indicating that the observed energy shifts are driven by differences in the ionization potentials of the μ_6 atom and not by subtle changes in the geometry of the cluster.

The sensitivity of XES to the identity of the bound ligands may be understood by more closely examining the electronic structure of the cluster (partially depicted in Figure 5). The occupied a_{1g} and t_{1u} bonding MOs are carbide-, nitrido-, or oxide-based MOs and therefore lie at very specific energies depending on the identity of the central species. This ultimately allows the partial fragment decomposition of the V2C XES spectrum of $[Fe_6C(CO)_{16}]^{2-}$, for which specific signatures for the C_{2p}- and C_{2s}-based MOs are obtained (Figure 6a; see also Figures S8−S10 and Tables S10−S14 for full fragment decompositions of all the investigated models). Conversely, the empty low-lying MOs (including the antibonding a_{1g}^* and t^*_{1u} of Figure 5) are primarily CO-based or Fe-based MOs and therefore relatively insensitive to changes in the central atom (consistent with the observed trends in the calculated Fe K-edge XAS pre-edges shown in Figure 2). Moreover, with the aid of DFT calculations and MOAnalyzer, we were able to obtain a decomposition of the full valence-to-core XES spectrum into the individual fragment contributions (see in addition to Figure 5, Tables S10−S14, and Figures S8−S10 in Supporting Information). A small

dx.doi.org/10.1021/ic201173j |*Inorg. Chem.* 2011, 50, 10709–10717

contribution to the spectrum was observed from $\pi_{2px,y}-\pi_{2px,y}$ CO-based MOs, particularly in those cases where the MOs are centered on carbonyls bridging two iron metals, notably C1−O1, C1A-O1A, C2−O2, and C3−O3 (see Table 1). More significantly, the two features lying in between C_{2s}- and C_{2p}-derived features (shown in orange in Figure 6) correspond to the σ^*_{2s-2s} and $\sigma_{2pz-2pz}$ CO-based orbitals, respectively, whereas the feature at higher energy, shown in blue, is due to Fe-3d based orbitals (Figure 6c). The latter arises due to significant Fe 3d−4p mixing which is promoted by the local symmetries around each iron.

CONCLUSION

In summary, we have demonstrated the ability of V2C XES to serve as a direct probe of the identity of light atoms within complex multimetallic frameworks, where characterization by crystallography and EXAFS presents significant challenges. The direct sensitivity of V2C XES to ligand ionization potential results in a ∼10 eV shift in a ligand 2s to metal 1s feature on going from C to N to O. In the case of a six iron cluster with a central carbide, the calculated features are faithfully reproduced within a simple DFT framework. The potential of XES to provide indirect supporting evidence for a given model has been highlighted. This study serves as a marker for future XES studies of small molecule interactions within multimetallic frameworks.

ASSOCIATED CONTENT

Supporting Information. Details for the crystallographic analysis at room and low temperatures; comparison of crystal structures and optimized geometries of $[Fe_6C(CO)_{16}]^{2-}$, $[Fe_6N(CO)_{16}]^{-}$ and $[Fe_6O(CO)_{16}]$; fits to the XES data using 5 and 6 peak models; comparison between the experimental XES data and calculated XES from additional models. This material is available free of charge via the Internet at http://pubs.acs.org.

AUTHOR INFORMATION

Corresponding Author

*E-mail: serena.debeer@mpi-mail.mpg.de.

ACKNOWLEDGMENT

S.D. thanks the Department of Chemistry and Chemical Biology at Cornell University for generous financial support. M.U.D.-J. thanks, in addition to the Department of Chemistry and Chemical Biology at Cornell, the National Council of Science and technology in Mexico (CONACyT) for complementary financial support. P.L.H. acknowledges funding from the NIH (GM065313). Portions of this research were carried out at the Stanford Synchrotron Radiation Lightsource, a national user facility operated by Stanford University on behalf of the DOE, BES. The SSRL SMB Program is supported by DOE, BER and NIH, NCRR, BMTP.

REFERENCES

(1) Kulkarni, A.; Lobo-Lapidus, R. J.; Gates, B. C. *Chem. Commun.* **2010**, *46*, 5997.
(2) Qiu, S.; Zhu, G. *Coord. Chem. Rev.* **2009**, *253*, 2891.
(3) Zhai, H.-J.; Wang, L.-S. *Chem. Phys. Lett.* **2010**, *500*, 185.
(4) Zhao, Q.; Betley, T. A. *Angew. Chem., Int. Ed.* **2011**, *50*, 709.
(5) Barman, S. F., H.; Blacque, O.; Venkatesan, K.; Yaghi, O. M.; Berke, H. *Chem. Commun.* **2010**, *46*, 7981.
(6) Chen, B.; Xiang, S.; Qian, G. *Acc. Chem. Res.* **2010**, *43* (8), 1115–1124.
(7) Deng, H.; Doonan, C. J.; Furukawa, H.; Ferreira, R. B.; Towne, J.; Knobler, C. B.; Wang, B.; Yaghi, O. M. *Science* **2010**, *327*, 846.
(8) Li, Q.; Zhang, W.; Miljanić, O. S.; Sue, C.-H.; Zhao, Y.-L.; Liu, L.; Knobler, C. B.; Stoddart, J. F.; Yaghi, O. M. *Science* **2009**, *325*, 855.
(9) Lee, N.; Petrenko, T.; Bergmann, U.; Neese, F.; DeBeer, S. *J. Am. Chem. Soc.* **2010**, *132*, 9715.
(10) Pollock, C. J.; DeBeer, S. *J. Am. Chem. Soc.* **2011**, *133*, 5594.
(11) Smolentsev, G.; Soldatov, A. V.; Messinger, J.; Merz, K.; Weyhermuller, T.; Bergmann, U.; Pushkar, Y.; Yano, J.; Yachandra, V. K.; Glatzel, P. *J. Am. Chem. Soc.* **2009**, 13161.
(12) Bergmann, U.; Horne, C. R.; Collins, T. J.; Workman, J. M.; Cramer, S. P. *Chem. Phys. Lett.* **1999**, *302*, 119.
(13) Lancaster, K. M.; Finkelstein, K. D.; DeBeer, S. *Inorg. Chem.* **2011**, *50*, 6767.
(14) Beckwith, M. A.; Roemelt, M.; Collomb, M. N.; DuBoc, C.; Weng, T. C.; Bergmann, U.; Glatzel, P.; Neese, F.; DeBeer, S. *Inorg. Chem.* **2011**, *50*, 8397.
(15) Churchill, M. R.; Wormold, J.; Knight, J.; Mays, M. Y. *J. Am. Chem. Soc.* **1971**, *93*, 3073.
(16) *Bruker SAINT*; Bruker AXS Inc.; Madison, Wisconsin, 2001.
(17) George, G. N. *EXAFSPAK, SSRL, SLAC*; Stanford University: Stanford, CA.
(18) Tenderholt, A. *PySpline*; Stanford Synchrotron Radiation Laboratory, Stanford Linear Accelerator Center, Stanford University: Stanford, CA.
(19) Mustre de Leon, J.; Rehr, J. J.; Zabinsky, S. I.; Albers, R. C. *Phys. Rev. B* **1991**, *44*, 4146.
(20) Delgado-Jaime, M. U.; Kennepohl, P. http://www.sourceforge.net/projects/blueprintxas, 2010.
(21) Delgado-Jaime, M. U.; Mewis, C. P.; Kennepohl, P. *J. Synchrotron Radiat.* **2010**, *17*, 132.
(22) Bitseff, D. http://leonardo.phys.washington.edu/feff/jfeff/.
(23) Glatzel, P.; Bergmann, U. *Coord. Chem. Rev.* **2005**, *249*, 65.
(24) Delgado-Jaime, M. U.; Kennepohl, P. *J. Synchrotron Radiat.* **2010**, *17*, 119.
(25) Neese, F. *Orca, an Ab Initio, Density Functional and Semiempirical Electronic Structure Program Package*, version 2.8; Universität Bonn: Bonn, Germany, 2010.
(26) DeBeer George, S.; Petrenko, T.; Neese, F. *J. Phys. Chem. A* **2008**, *112*, 12936.
(27) Becke, A. D. *Phys. Rev. A* **1988**, *38*, 3098.
(28) Perdew, J. P. *Phys. Rev. B* **1986**, *33*, 8822.
(29) Perdew, J. P. *Phys. Rev. B* **1986**, *34*, 7406.
(30) van Wüllen, C. J. *Chem. Phys.* **1998**, *109*, 392.
(31) Neese, F. *Inorg. Chim. Acta* **2002**, *337C*, 181.
(32) Klamt, A.; Schürmann, G. *J. Chem. Soc., Perkin. Trans.* **1993**, *2*, 799.
(33) Delgado-Jaime, M. U.; DeBeer, S. http://www.sourceforge.net/projects/moanalyzer, 2011.
(34) Pettersen, E. F.; Goddard, T. D.; Huang, C. C.; Couch, G. S.; Greenblatt, D. M.; Meng, E. C.; Ferrin, T. E. *J. Comput. Chem.* **2004**, *13*, 1605.
(35) Rehr, J. J.; Villa, F.; Prange, M.; Kas, J.; Takimoto, Y.; Sorini, A.; Jorissen, K; Soininen, A.; Ankudinov, A.; Ahmed, T. *FEFF Project*; http://leonardo.phys.washington.edu/feff/.
(36) Churchill, M. R.; Wormald, J. *J. Chem. Soc., Dalton Trans.* **1974**, 2410.
(37) Lopatin, V. E.; Varnek, V. A.; Belskii, V. K. *J. Struct. Chem.* **2002**, *43*, 608.
(38) Berry, J. F.; DeBeer George, S.; Neese, F. *Phys. Chem. Chem. Phys.* **2008**, *10*, 4361.
(39) Olah, G. A.; Surya-Prakash, G. K.; Williams, R. E.; Field, L. D.; Wade, K. In *Hypercarbon Chemistry*; John Wiley & Sons: New York, 1987, p 123.
(40) Stone, A. J. *Polyhedron* **1984**, *3*, 1299.
(41) Whelan, T.; Brint, P. *J. Chem. Soc., Faraday Trans. 2* **1985**, *81*, 267.

(42) Bergmann, U.; Glatzel, P.; Robblee, J. H.; Messinger, J.; Fernandez, C.; Roehl, C.; Visser, H.; McFarlane, K.; Bellacchio, E.; Pizarro, S.; Sauer, K.; Yachandra, V. K.; Klein, M. P.; Cox, B. L.; Nealson, K. H.; Cramer, S. P. *J. Synchrotron Radiat.* **2001**, *8*, 199.

(43) Eeckhout, S. G.; Safonova, O. V.; Smolentsev, G.; Biasioli, M.; Safonov, V. A.; Vykhodtseva, L. N.; Sikora, M.; Glatzel, P. *J. Anal. At. Spectrom.* **2009**, *24*, 215.